Free-Surface Characteristics of a Liquid Li Wall Jet*)

Takuji KANEMURA[a)], Hiroo KONDO[b)], Hirokazu SUGIURA[1,c)], Sachiko YOSHIHASHI[1,d)], Eiji HOASHI[1)], Takeo MUROGA[2)], Tomohiro FURUKAWA, Yasushi HIRAKAWA, Eiichi WAKAI and Hiroshi HORIIKE[1,e)]

Japan Atomic Energy Agency, Oarai, Ibaraki 311-1393, Japan
[1)]*Osaka University, Suita, Osaka 565-0871, Japan*
[2)]*National Institute for Fusion Science, Toki, Gifu 509-5292, Japan*

(Received 20 February 2016 / Accepted 28 July 2016)

In this study, the free-surface characteristics of a liquid Li wall jet for the Li target of the International Fusion Materials Irradiation Facility (IFMIF) are comprehensively reviewed. In developing the IFMIF Li target, a scientific understanding of the free-surface wave characteristics and the development of diagnostic tools to measure these characteristics were critical issues. The same issues must be faced in other liquid metal applications in fusion engineering, such as liquid first walls or liquid diverters. Thus far, diagnostic tools and methods to measure all of the characteristics of waves (i.e., wavelength, wave period, wave speed (free-surface speed), wave height (amplitude)), and average jet thickness have been developed, and the probability distributions applicable to these wave parameters, as well as their statistical characteristic values, have been determined, validating the stability of the IFMIF Li target. Our findings, both the wave characteristics and the diagnostic tools, can be applied to not only the IFMIF Li target but also innovative liquid metal diverters or first walls in fusion engineering.

Keywords: liquid metal, Li, wall jet, flow characteristic, free surface, IFMIF, diagnostic tool

DOI: 10.1585/pfr.11.1405117

1. Introduction

1.1 Liquid-metal free-surface flow applications in fusion engineering

Liquid metals interest fusion science researchers engaged in developing innovative fusion-related devices, such as the first walls of inertial confinement fusion reactors [1, 2] and magnetic confinement fusion reactors [3, 4], diverters [5], blankets [6], and liquid Li target flow at the International Fusion Materials Irradiation Facility (IFMIF) [7]. The removal of the ultra-high heat loads from plasmas and beams is a crucial engineering issue in such devices. Liquid metals can receive high heat loads from plasma or beams because liquid metals have wide temperature ranges between their melting and boiling points and high thermal conductivities. Liquid metals have received considerable attention as heat removal media, and researchers have proposed liquid-metal free-surface flow over a structural material (solid) in such devices. The flow can be exposed to vacuum or plasma directly without a window material.

We are involved in the development of the liquid Li target at IFMIF. IFMIF has an accelerator-based intense neutron source that uses Li(d,xn) reactions where a high-speed Li jet is bombarded by two 40 MeV and 125 mA deuteron beams (total beam power: 10 MW). The Li jet is called the Li target. It flows in a vacuum of 10^{-3} Pa with no beam window so that it can exist in the beam path. The flow stability of the Li target is crucial for IFMIF. A 40 MeV deuteron penetrates 22 mm into the Li target. Accordingly, the thickness of the Li target must be greater than 22 mm to stop the beams completely. To ensure safety, the Li target should be as thick as possible. From the viewpoint of neutron transport, neutrons must not be decelerated in the target; therefore, the Li thickness should be as thin as possible. Considering these requirements, the Li target thickness is determined to be 25 mm. The permissible non-uniformity is defined as ±1 mm in thickness. The design requirements (specifications) of the Li target are listed in Table 1. IFMIF is now in the Engineering Validation and Engineering Design Activities stage (called the IFMIF/EVEDA project) [8]. This project is being jointly pursued by Japan and Europe.

1.2 Issues pertaining to liquid-metal free-surface flow applications

In general, liquid metals are used at high temperatures. Corrosion and erosion damage of structural materials must be reduced to ensure long-term system integrity. In particular, when using liquid Li, a popular metal in fusion en-

author's e-mail: kanemura@frib.msu.edu
[a)] *Currently Michigan State University*
[b)] *Currently National Institutes for Quantum and Radiological Science and Technology*
[c)] *Currently Mitsubishi Heavy Industries Ltd.*
[d)] *Currently Nagoya University*
[e)] *Currently Fukui University of Technology*
[*)] This article is based on the invited talk at the 32nd JSPF annual meeting (2015, Nagoya).

Table 1 Primary requirements of the IFMIF Li target.

Parameter	Values	Notes
Heat load	10 MW	Averaged heat flux: 1 GW/m^2 (Deuteron beam footprint: 50 mm height × 200 mm width)
Jet velocity	15 m/s	Range: 10–16 m/s
Jet thickness	25 mm	Variation: ±1 mm
Jet width	260 mm	
Initial (inlet) Li temperature	250 °C	Melting point of Li: 180.5 °C
Vacuum pressure	10^{-3} to 10^{-2} Pa	Near Li free surface

Table 2 Diagnostic tools and methods of measuring Li free-surface flow characteristics.

Tools/methods	Type	Measuring objects
Common video camera	Imaging device (non-contact)	Flow appearance
High-speed video (HSV) camera	Imaging device (non-contact)	Flow appearance, wavelength
Contact-type liquid level sensor (contact probe)	Contact	Wave height (amplitude), wavelength, wave period, average flow thickness
Laser probe (LP) method	Non-contact	Wave height (amplitude), average flow thickness
Pattern projection method	Non-contact	Wake shape
Surface-wave tracking (SWAT) method	Non-contact	Wave speed (free-surface speed)

gineering, its high chemical reactivity needs to be considered.

When considering the use of a liquid metal in a magnetic confinement fusion reactor (e.g., a liquid metal first wall), it is necessary to overcome the magnetohydrodynamic (MHD) pressure loss in high-level magnetic fields. A possible countermeasure is to coat the piping with an electrical insulation film.

In addition, scientific understanding of the free-surface stability is important. If liquid metal flow is used in the diverter or the first wall to cover structural materials and to mitigate heat flux, the flow has a free surface, and free-surface fluctuations due to surface waves or free-surface turbulence need to be measured to understand their characteristics as design input data for device development. Accordingly, the development of diagnostic tools to measure liquid metal free-surface conditions is crucial. Diagnostic tools developed for water flow cannot be applied, primarily due to liquid metals' opacities, specularities, and high operating temperatures (the high chemical reactivity of Li). Thus, special diagnostic methods of measuring these characteristics must be developed. This is a common issue in the development of liquid-metal free-surface flow applications in fusion-related devices.

1.3 Study purpose

As stated above, the development of relevant diagnostic tools and gaining scientific understanding of liquid-metal free-surface flow characteristics are common issues in the development of liquid-metal free-surface flow applications in fusion-related devices and facilities (the MHD problem is only related to magnetic confinement fusion reactors, not to inertia confinement reactors or the IFMIF Li target).

In this study, we focus on these two issues. We are involved in the development of the IFMIF Li target. We have developed diagnostic tools to measure the properties of the Li target flow and have measured and examined these properties using the developed tools. In this study, we review our findings that are related to the properties of the Li target flow. We believe that our results will contribute to the advancement of liquid metal applications in fusion engineering.

2. Diagnostic Tools for Liquid-Metal Free-Surface Flow

Table 2 lists the diagnostic tools and methods developed or employed by us for a Li jet. They are classified into three categories: 1) imaging devices, 2) contact-type sensors, and 3) non-contact-type sensors. In this section, we briefly outline these categories. Detailed information concerning the diagnostics and methods is provided in Sec. 4 and in the references.

2.1 Imaging devices

A generic video camera is useful to monitor flow visually during an experiment. The camera obtains images of the flow continuously. However, the frame rate of a generic video camera is not high (usually approximately 30 frames per second (fps)). Therefore, it is not possible to capture high-speed phenomena occurring at frequencies greater than 30 fps.

A high-speed video (HSV) camera can overcome this problem. We used Photron Fastcam SA 1.1, SA-5, and SA-X HSV cameras. These cameras can achieve the frame rates required to visualize free-surface waves on a Li jet of up to 20 m/s. However, depending on the frame rate selected, the recording time can be as low as 1 s.

2.2 Contact-type diagnostic tools

A contact-type liquid level sensor (a contact probe) detects contact signals between the probe and the Li surface, and the detected signals can be used to analyze the free-surface fluctuation characteristics statistically [9–12]. The obtained characteristics are the wave period, wavelength, and wave height (amplitude) of the free-surface fluctuations. The greatest benefit of this method is that it enables the probability distributions and statistical values of the abovementioned characteristics to be obtained. We introduced the log–normal distribution for the wave period and wavelength distributions and the Rayleigh distribution for the wave height distribution. We demonstrated, for the first time, that the measurement results of the Li jet agreed well with the abovementioned probability distributions. These distributions were derived from the random-phase/amplitude model of ocean waves (the model is described in Sec. 4.3). Therefore, the measured free-surface fluctuations of the Li jet were determined to be stochastically random phenomena.

2.3 Non-contact-type diagnostic tools and methods

There are a few non-contact-type diagnostic tools or methods.

The laser probe (LP) method [13, 14] is a laser-based non-contact method that can be used to measure jet thickness and wave height. We developed the LP method following the analysis method (zero-up crossing method) used in the random-phase/amplitude model, which is also employed in the contact probe method. The biggest advantage of the LP method is that the Li jet thickness and free-surface fluctuations can be measured with high precision and accuracy from a long distance (in a contactless manner).

The pattern projection method can be used to measure the three-dimensional (3D) shape of an object based on the Fourier-transform profilometry method. We used this method to measure the shapes of free-surface wakes generated at the nozzle edge [15].

The surface-wave tracking (SWAT) method is based on the particle image velocimetry (PIV) technique, which is typically applied to water (a transparent fluid) to measure two-dimensional (2D) or 3D velocity fields using cross-correlation values in the two interrogation regions of the double-image seeding tracer particles. PIV is a powerful method of investigating flow fields; however, it has a fundamentally unavoidable problem regarding its application to Li flow, which is that tracer particles cannot be seeded into a Li circulation loop. Therefore, we developed a SWAT method to measure the surface-wave velocities. The developed SWAT method enables the measurement of 2D surface-wave velocity distributions via cross-correlation analysis of the intensity patterns generated by free-surface waves without seeding tracer particles [16–18].

3. Experimental Facilities

This section describes two experimental facilities where we conducted experiments, namely, the Osaka University Li loop and the EVEDA Li test loop (ELTL). In the framework of the key element technology phase (KEP) of IFMIF, which lasted from 2000 until 2002, the former Osaka University Li loop [19] was modified to perform experiments on a high-speed (up to 16 m/s) liquid Li jet simulating the IFMIF Li target [20]. After successful experiments in the Osaka University Li loop, ELTL was constructed in the Oarai R&D center of the Japan Atomic Energy Agency in the framework of the IFMIF/EVEDA project.

3.1 Osaka University Li loop

Figure 1 shows the piping and instrumentation diagram (P&ID) of the Osaka University Li loop. The Li inventory is 420 l. The main loop consists of an annular linear induction pump-type electromagnetic pump (EMP),

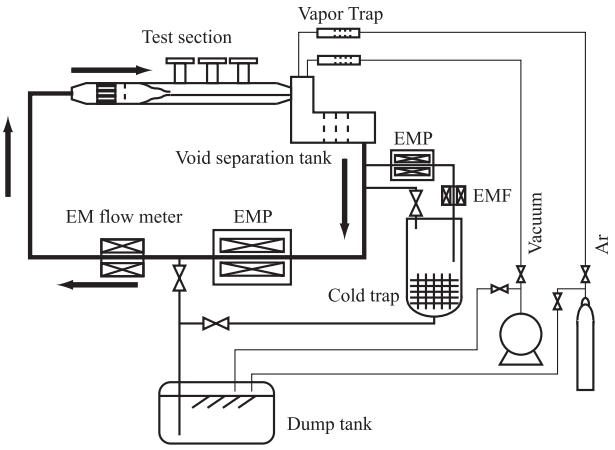

Fig. 1 Piping and instrumentation diagram of the Osaka University Li loop. The bold line shows a main circulation pipe, with arrows indicating the flow direction. The cold trap is a purification device using the precipitation of impurities oversaturated in the cooled liquid Li.

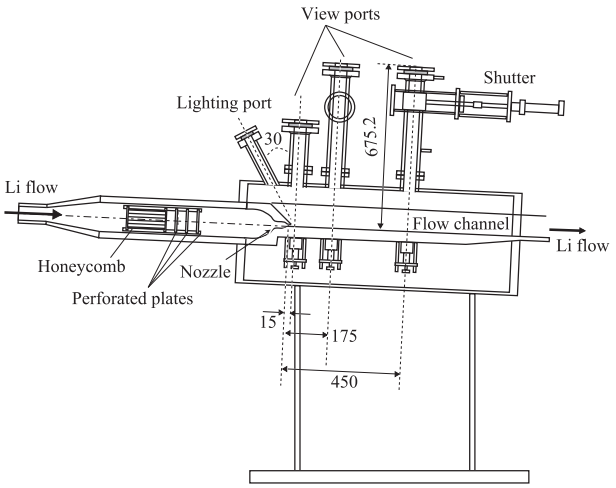

Fig. 2 Configuration of the test section of the Osaka University Li loop. Li pumped by the EMP flows into the test section. A wall jet is generated along a straight horizontal 70-mm-wide flow channel after the Li passes through a honeycomb, three perforated plates, and a nozzle.

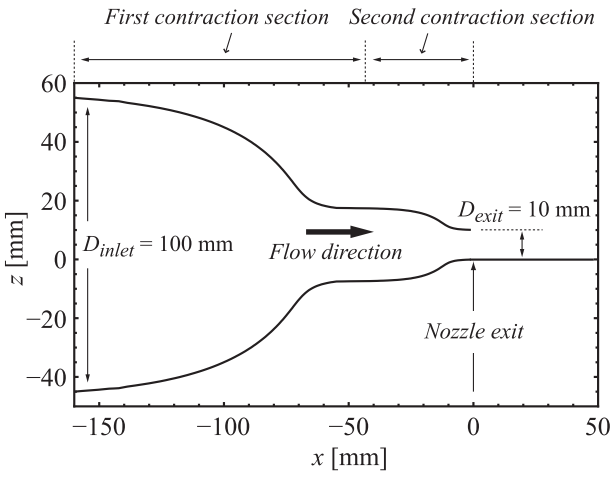

Fig. 3 Cross-sectional drawing of the nozzle of the Osaka University Li loop. This two-stage contraction nozzle is a 1/2.5 scale model of the IFMIF nozzle [21, 22]. The total contraction ratio is 10. The nozzle exit is smoothly connected to the horizontal flow channel.

an electromagnetic flow meter (EMF), two test sections for heat transfer under transverse magnetic fields and for high-speed jets (only the test section for the high-speed jet is shown), and a void separation tank. These components are connected by 2-inch-diameter 304 stainless steel pipes. The maximum flow rate of the EMP is 670 l/min, corresponding to a jet speed of 16 m/s at the test section. Here the mean jet speed (U_{m}) is calculated by dividing the flow rate (F) by the cross-sectional area (A) of the nozzle outlet ($U_{\mathrm{m}} = F/A$). In IFMIF, Li flows in a vacuum. In contrast, the Osaka University Li loop is operated in an Ar atmosphere of 0.12 - 0.15 MPa because cavitation occurs at the suction side of the EMP due to the insufficient gravity head from the void separation tank to the EMP if the loop is operated in a vacuum. The operating temperature is 300 °C to prevent the Li from accidentally freezing (the melting point of Li is 180.7 °C).

The configuration of the test section for high-speed jet experiments is shown in Fig. 2. The test section is composed of a flow straightener (a honeycomb and three perforated plates), a two-stage contraction nozzle, and a 70-mm-wide straight flow channel. The flow channel is placed horizontally to vary the velocity from stagnant to > 15 m/s and is incorporated into a vacuum chamber equipped with three view ports from which to observe or measure the Li jet. The nozzle has two contraction sections, as shown in Fig. 3. The nozzle of the Osaka University Li loop is a 1/2.5 scale model of the IFMIF nozzle. The thickness and width of the Li target at the nozzle exit are 10 mm and 70 mm, respectively. The design of the IFMIF nozzle was formulated during the conceptual design activities phase of IFMIF [21, 22]. The contraction ratios of the first and second parts are 4 and 2.5, respectively.

Table 3 Re, We, and Fr numbers for the Osaka University loop.

$Re(= LU/\nu)$	1.5×10^5
$We(= \rho LU^2/\sigma)$	3.0×10^3
$Fr\ (= U^2/gL)$	2.3×10^3
Note	ν: dynamic viscosity ρ: density σ: surface tension g: gravity acceleration U(characteristic velocity) = 15 m/s L(characteristic length) = 10 mm Physical properties of Li at 300 °C

Table 3 lists the Reynolds (Re), Weber (We), and Froude (Fr) numbers under typical experimental conditions (a jet speed of 15 m/s). These dimensionless numbers, employed in fluid mechanics, are useful when analyzing free-surface flows. The Re number is defined as the ratio of the inertial forces to the viscous forces and consequently quantifies the relative importance of these two types of forces. When the Re number is low, viscous forces are dominant and laminar flow occurs. In contrast, when the Re number is high, inertial forces are dominant and turbulent flow occurs. The We number is used as a measure of the relative importance of a fluid's inertia compared to its surface tension. The Fr number is used as a measure of the relative importance of a fluid's inertia compared to an external field (e.g., the gravitational field). When the We and Fr numbers are high, restoring forces acting on the free surface (e.g., the surface tension and gravity) are weak compared to the inertial forces, and the free surface fluctuates. All of the numbers in Table 3 are very large, suggesting that the jet is in a turbulent condition and that the jet's free surface is not smooth.

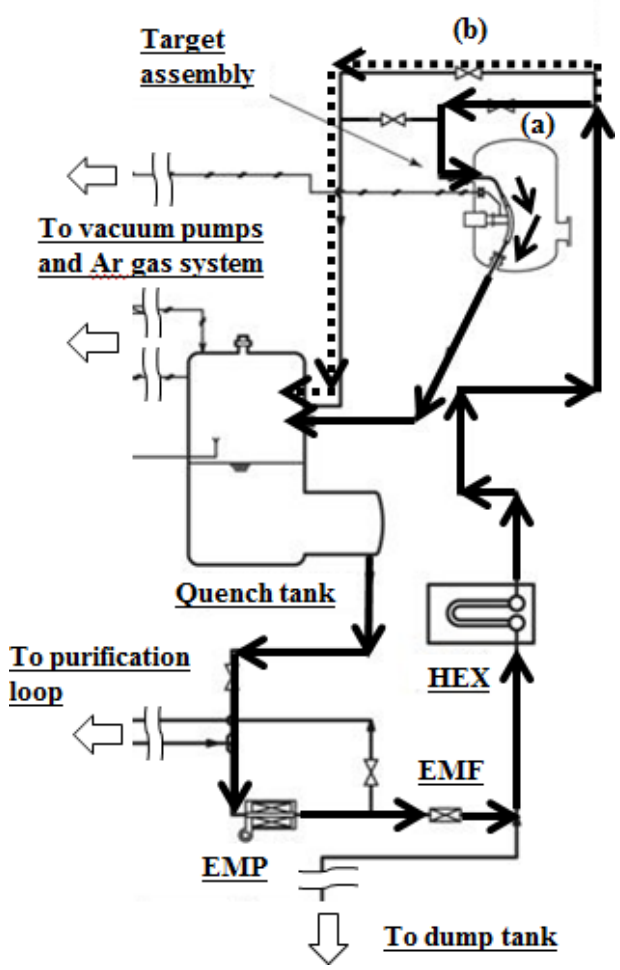

Fig. 4 Piping and instrumentation diagram of the ELTL main loop. The main Li path is indicated by the solid arrows. TA is located at the top of the loop inside the confinement vessel. The path of the dotted line arrows, indicated by (b), shows the flow line bypassing the TA.

3.2 ELTL

Figure 4 shows the P&ID of the main loop of ELTL. The Li inventory in ELTL is 5 m^3 (5000 l), and the platform size of ELTL is roughly 20 m × 20 m × 20 m. The detailed design of ELTL is described in Refs. [23–27]. The main Li loop was designed to supply liquid Li to the target assembly (TA) where the Li target is produced. The main loop consists of 6-inch pipes made of AISI-type 304 stainless steel, the TA, a quench tank, an EMP, an EMF, a heat exchanger (HEX), and valves. The tanks are connected to an Ar gas supply system and vacuum pumps to control the pressure and for evacuation. The main loop of ELTL has two flow paths: (a) a flow path through the TA (denoted by the bold arrows) and (b) a flow path bypassing the TA (denoted by the dotted arrows). The maximum flow rate of the EMP is 0.05 m^3/s (3000 l/min), corresponding to a Li target speed of 20 m/s. The operational temperature and Ar pressure range from 250 °C to 350 °C and from 10^{-3} Pa to 0.12 MPa, respectively.

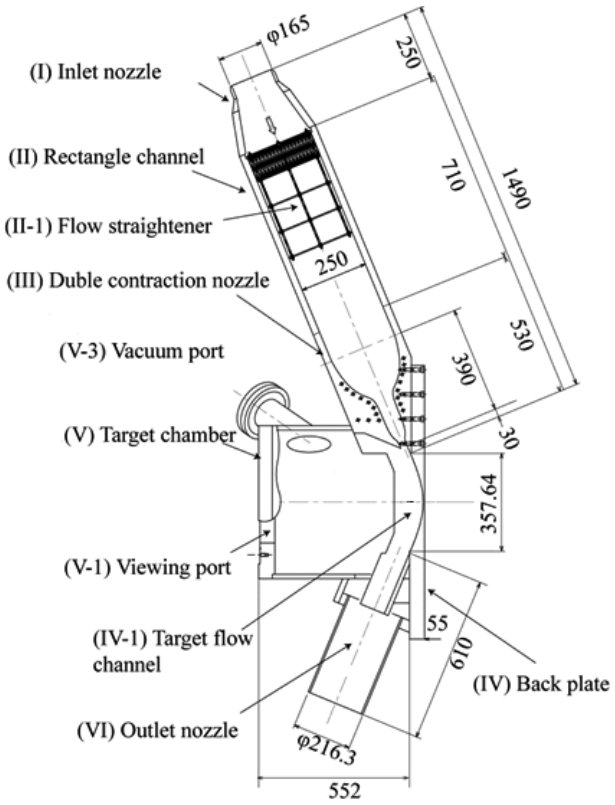

Fig. 5 TA configuration. The design of the ELTL TA is identical to that of the IFMIF TA except for the width of the flow channel (ELTL: 100 mm, IFMIF: 260 mm). The components of the TA are nearly the same as those of the Osaka University Li loop test section. The main differences between them are the flow channel orientation and the curvature.

Table 4 Re, We, and Fr numbers for ELTL.

$Re(= LU/\nu)$	3.5×10^5
$We(= \rho LU^2/\sigma)$	7.4×10^5
$Fr\ (= U^2/a_c L)$	10
Note	ν: dynamic viscosity ρ: density σ: surface tension a_c: centrifugal acceleration (U^2/R, R: curvature radius of back plate) U(characteristic velocity) = 15 m/s L(characteristic length) = 25 mm Physical properties of Li at 250 °C

Figure 5 shows the configuration of the TA. The major components of the TA are a flow straightener (II-1), double contraction nozzle (III), and back plate (IV) [23]. Liquid Li supplied to the TA flows through the contraction nozzle, and the Li target flow (wall jet) is formed along the back plate. The thickness and width of the Li target at the nozzle exit are 25 mm and 100 mm, respectively. Only the width is scaled down from 260 mm to 100 mm compared to that of IFMIF (see Table 1). The Li target can be observed and measured in detail through a viewing port (V-1).

Table 4 lists the Re, We, and Fr numbers under typical

experimental conditions (a jet speed of 15 m/s) at ELTL. The *Re* and *We* numbers are comparable to those of the Osaka University loop; however, the Fr number is much smaller than that of the Osaka University loop. This is because the acceleration perpendicular to the flow direction (a) is different in the two cases. For the Osaka University loop, a is the gravitational acceleration (g). In contrast, for ELTL, a is the centrifugal acceleration (a_c). Interestingly, the Fr number is independent of flow velocity for ELTL ($Fr = U^2/a_c L = R/L$). Therefore, if the stability of the Li target in ELTL depends on the Fr number, it can be expected that the stability will remain unchanged even when the flow velocity is changed.

4. Flow Characteristics

This section summarizes our results, including some new experimental results obtained from ELTL, from the viewpoint of the wave characteristics (i.e., wavelength, wave speed, wave period, and wave height (amplitude)) and the average target thickness. In addition, the measurement and analysis methods are described.

4.1 Wavelength and flow appearance

Wavelengths are measured using an image measurement technique. Therefore, selecting a suitable camera is important. A camera with a wide dynamic range in terms of color tone needs to be selected because the liquid metal free surface is specular.

In our previous experiments, free-surface pictures were captured using a charge-coupled device camera (Sensicam qe, PCO AG) and a stroboscopic light source with a short light emission pulse of 20 µs. Figure 6 shows three images of liquid Li free surfaces near the nozzle exit at velocities of 3 m/s, 7 m/s, and 13 m/s that were obtained in the Osaka University loop [28]. At lower velocities, the surface was fully smooth and few waves were generated on the surface, as shown in Fig. 6 (a). At velocities of 5 - 8 m/s, periodic 2D waves were observed a short distance from the nozzle exit, as shown in Fig. 6 (b). Similar periodic waves were observed on a water jet free surface by Itoh [29] and on a Li jet surface by Hassberger [30]. These periodic waves are generated due to the instability of the shear layer existing underneath the free surface immediately after the nozzle exit [31]. In other words, the existence of these periodic waves indicates that the boundary-layer flow at the nozzle exit is still laminar. At velocities greater than 9 m/s, no 2D waves were observed and the surface was covered by irregular waves, as shown in Fig. 6 (c). In this velocity range, the boundary-layer flow at the nozzle exit is turbulent, according to Ref. [29]. The aforementioned free-surface observations made in our experiment are consistent with the results given in Ref. [29]. The wavelengths of the periodic 2D waves near the nozzle exit were measured from the images, and their dependence on the *We* number was examined. The experimental results

(a)

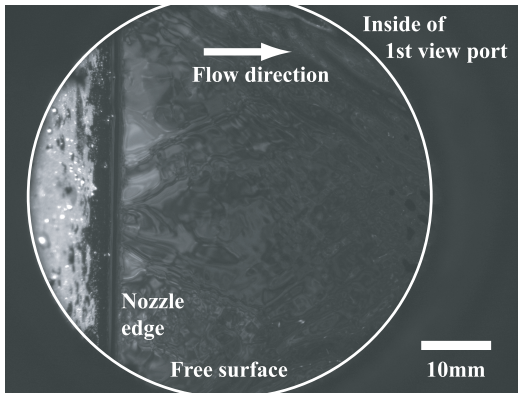

(b)

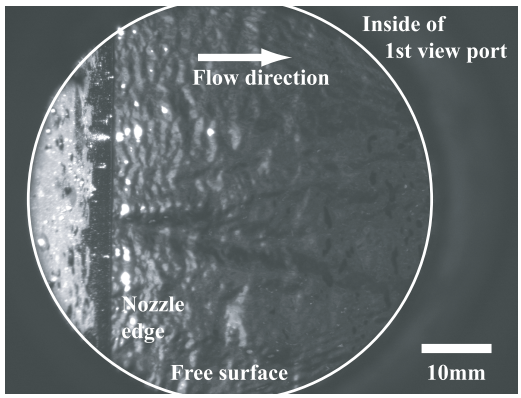

(c)

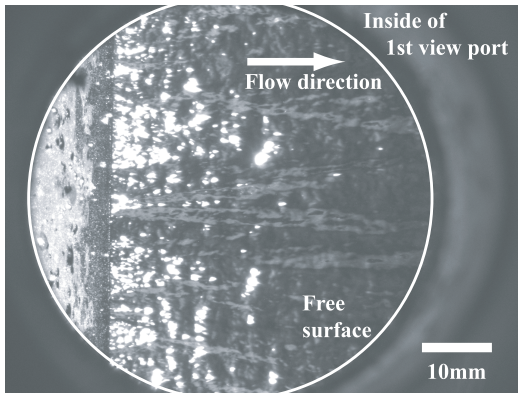

Fig. 6 Image of the Li free surface obtained at the Osaka University loop: (a) $\boldsymbol{U}_\mathbf{m}$ = 3 m/s, (b) $\boldsymbol{U}_\mathbf{m}$ = 7 m/s, and (c) $\boldsymbol{U}_\mathbf{m}$ = 13 m/s. These images were taken from the view port above the nozzle. Li flows rightward. At $\boldsymbol{U}_\mathbf{m}$ = 3 m/s, no traveling waves are observable (laminar flow occurs at the nozzle exit). At $\boldsymbol{U}_\mathbf{m}$ = 7 m/s, small periodic traveling waves are evident just after the nozzle edge (laminar flow still occurs at the nozzle exit). At $\boldsymbol{U}_\mathbf{m}$ = 13 m/s, only irregular waves are observable on the entire free surface (turbulent flow occurs at the nozzle exit). The dependence of the free surface appearance on the flow speed provides information about the change in the flow conditions at the nozzle exit.

agreed closely with those predicted using the linear stability theory of a shear layer underneath a free surface [28]. This agreement clearly indicates that the dominant restoring force acting on the waves is the surface tension, not gravity.

In recent experiments, we used an HSV camera (Fastcam SA series, Photron Limited) to visualize and examine the free-surface appearance of a Li jet in detail [32]. In general, HSV cameras have many advantages compared to still cameras when examining random phenomena such as irregular free-surface waves.

Note that the primary purposes of flow observation are to define the objects to be measured (the free-surface phenomena) and to estimate their temporal and spatial scales. In our case, the free-surface phenomena are traveling irregular free-surface waves (wavelength: mm-order, frequency: kHz-order, amplitude: sub-mm-order) and stationary surface wakes (amplitude: mm-order). From this viewpoint, an appropriate imaging device can be selected depending on the purpose of the observation. For instance, a normal video camera is suitable for continuously monitoring flow behavior, while a still camera with a long exposure time can produce a time-averaged flow appearance. Long-exposure photographs clearly reveal the existence of stationary surface wakes originating at the nozzle corners between the nozzle edge and both side walls [33–35].

Wavelengths can also be measured using a contact probe [11]. The dominant wavelengths measured using the contact probe agreed well with those obtained from the image measurements. In addition, the obtained wavelength distribution agreed well with the log–normal distribution.

4.2 Wave speed

Wave speeds can be measured using our developed SWAT method [16–18]. This SWAT method is based on the PIV technique, which is typically applied to water (a transparent fluid) to measure a 2D or 3D velocity field using cross-correlation values in two interrogation regions of double-images seeding tracer particles. PIV is a powerful method of investigating flow fields; however, it has a fundamentally unavoidable problem when applied to Li flow, that is, tracer particles cannot be seeded into a Li circulation loop. Therefore, we developed a SWAT method to measure the surface-wave velocities.

The developed SWAT method enables 2D surface-wave velocity distributions to be measured via cross-correlation analysis of the intensity patterns generated by the free-surface waves without the necessity of seeding tracer particles. The measurement procedure of the developed SWAT method is described and shown in Ref. [17]. By analyzing a pair of images taken sequentially at a time interval of Δt, the movement vector ($\boldsymbol{d}$) at a given measurement point can be obtained. Therefore, the velocity vector ($\boldsymbol{u}$) can be calculated as follows:

$$\boldsymbol{u} = \alpha \frac{\boldsymbol{d}}{\Delta t}, \tag{1}$$

where α is the image scale (m/pixel). Furthermore, subpixel analysis was employed to improve the measurement resolution, which is defined as $0.1\alpha/\Delta t$ [17].

The following two points must be emphasized when the SWAT method is used.

The first point involves the relationship between the surface-wave velocity (u_{wave}) and the surface velocity of the jet (u_{s}). In principle, u_{wave}, not u_{s}, is measured in the SWAT method. When the free-surface flow is laminar, u_{wave} is separable into the jet surface velocity and the phase speed of the waves (c_{wave}), i.e., $u_{\mathrm{wave}} = c_{\mathrm{wave}} + u_{\mathrm{s}}$. In a study conducted in the Osaka University Li loop [16], we experimentally proved that the above relationship ($u_{\mathrm{wave}} = c_{\mathrm{wave}} + u_{\mathrm{s}}$) holds when $U_{\mathrm{m}} \leq 8$ m/s. In this velocity range, the free surface of a Li flow produced by an IFMIF-type nozzle is laminar, as mentioned in Sec. 4.1. In contrast, at higher velocities (e.g., $U_{\mathrm{m}} \geq 10$ m/s), the boundary layer at the nozzle exit becomes turbulent and the produced free-surface is turbulent [29]. In this case, the free-surface fluctuations are no longer waves but are instead caused by turbulent fluid motions beneath the free surface, and irregular patterns appearing on the free surface travel at the surface velocity with zero or negligible phase velocity (i.e., $u_{\mathrm{wave}} \approx u_{\mathrm{s}}$). In another study [17], it was experimentally proven that this relation ($u_{\mathrm{wave}} \approx u_{\mathrm{s}}$) holds when $U_{\mathrm{m}} \geq 10$ m/s.

The second point concerns the effect of surface wakes on the measurement results. It has been found that, if a surface wake exists inside a measurement area, the measured velocity vectors are directed toward the edge lines of the surface wakes and that their magnitudes are reduced (5% - 10%) compared to U_{m} [17]. This reduction may be caused by the secondary flow induced by the surface wake. When using the SWAT method, the measured velocity ($\boldsymbol{u}$) is assumed to have only x and y components and not a z component, i.e., $\boldsymbol{u} = u_x\boldsymbol{i}_x + u_y\boldsymbol{i}_y$. If a relatively large locally stationary free-surface deformation induced by the surface wake exists, the velocity near that deformation always has three components and is expressed as $\boldsymbol{u} = u_x\boldsymbol{i}_x + u_y\boldsymbol{i}_y + u_z\boldsymbol{i}_z$. This deformation results in the measured velocities being lower than the actual surface velocities. The actual relationship between the measured velocity and the surface velocity in such cases is presently unknown. Therefore, it is necessary to eliminate or essentially overlook results measured in the region in which a surface wake exists.

Figure 7 shows the surface velocities near the nozzle exit obtained at the Osaka University loop under laminar conditions ($U_{\mathrm{m}} \leq 8$ m/s) using the relationship $u_{\mathrm{s}} = u_{\mathrm{wave}} - c_{\mathrm{wave}}$ [16]. In Fig. 7, the horizontal axis X indicates a dimensionless length scale, where x is the distance from the nozzle exit, δ_2 is the momentum thickness at the nozzle exit, and Re_{δ_2} is the Re number based on the mainstream velocity (U_{m}) and the momentum thickness (δ_2). For comparison, the surface velocities of a water jet measured using laser Doppler velocimetry [29] are also shown in Fig. 7. u_{s} is zero at the nozzle exit because any fluid motions contact-

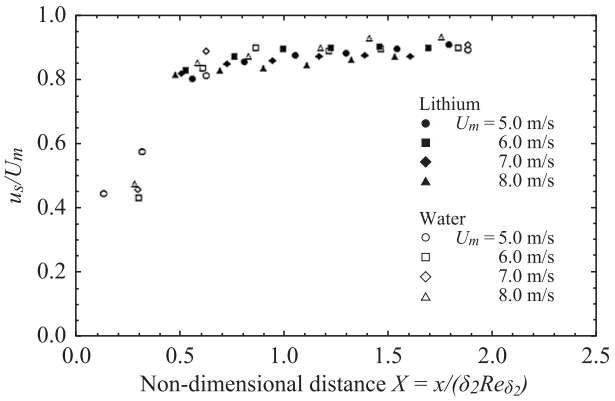

Fig. 7 Surface velocity obtained under laminar conditions at the Osaka University loop. The filled-in symbols indicate the experimental data obtained at the Osaka University loop; the empty symbols indicate the experimental data obtained at a water loop, the test section of which has almost the same configuration as the Osaka University loop test section [29]. X is a dimensionless length scale, x is the distance from the nozzle exit, δ_2 is the momentum thickness at the nozzle exit, and Re_{δ_2} is the Re number based on the mainstream velocity (U_m) and the momentum thickness (δ_2).

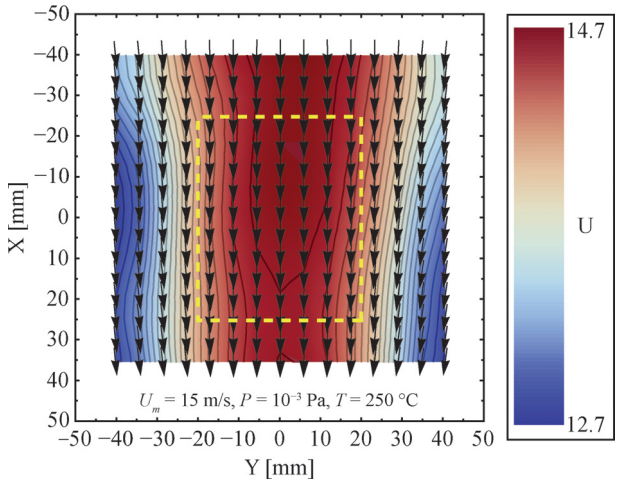

Fig. 8 Two-dimensional surface velocity obtained at $\boldsymbol{U}_\mathbf{m}$ = 15 m/s at ELTL. The origin (X, Y) = (0, 0) represents the IFMIF beam center. The yellow dashed rectangle shows the corresponding IFMIF beam footprint. The side walls are located at Y = ±50 mm. The arrows indicate the directions of the Li surface velocity vectors. The contour shows the norm of the velocity vectors.

ing a wall are bound to the wall motions due to the fluid's viscosity; if the nozzle remains stationary, the fluid speed along the nozzle's inner wall is zero. After the fluid is separated from the nozzle wall, a free surface is formed and accelerates due to viscosity, and the free-surface velocity (u_s) approaches the mainstream velocity (U_m). As shown in Fig. 7, both Li and water rapidly accelerate a short distance from the nozzle exit, and after this rapid acceleration, u_s gradually approaches U_m. The results for Li and water show similar trends due to Reynolds' law of similarity.

Figure 8 shows the 2D velocity distribution for the velocity vectors measured at U_m = 15 m/s at ELTL [18]. The relationship $u_\mathrm{wave} \approx u_\mathrm{s}$ holds at this speed. The contour indicates the norm of the velocity vectors: $U = \|\boldsymbol{u}\| = \sqrt{u_x^2 + u_y^2}$. The origin (X,Y) = (0,0) corresponds to the deuteron beam center in IFMIF (approximately 200 mm downstream from the nozzle exit). Li flows in the positive X direction, and the side walls are located at Y = ±50 mm. The region inside the rectangle, drawn with a yellow dashed line, corresponds to the IFMIF beam footprint. The velocity distribution is sufficiently uniform for IFMIF, and the free-surface speed is nearly equal to U_m in this region. The free-surface speed measured at (X,Y) = (0,0) closely agrees with the analytically predicted value [18]. In contrast, the effect of the surface wakes generated at the corners between the nozzle edge and the side walls can be seen clearly near both of the side walls and is consistent with the results of visual observations [18].

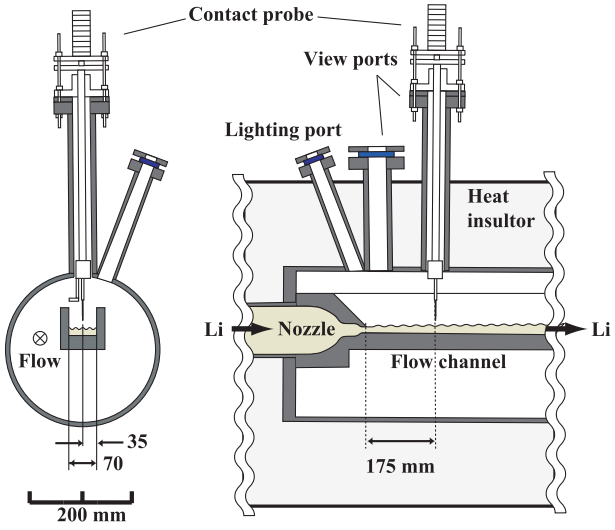

Fig. 9 Experimental setup of the contact probe at the Osaka University loop. The measurement probe is installed 175 mm downstream from the nozzle and 35 mm from the two side walls. This location corresponds approximately to the IFMIF beam center.

4.3 Wave period

Wave periods can be measured using contact probes.

Figure 9 shows the experimental setup of the contact probe at the Osaka University loop. The contact probe is equipped with a probe and a stepper motor to drive the probe vertically. Contact signals are detected as the voltage drops from 5 V to 0 V when the probe comes into contact with the Li surface. The probe is scanned vertically step by step using the stepper motor, and the contact signals are

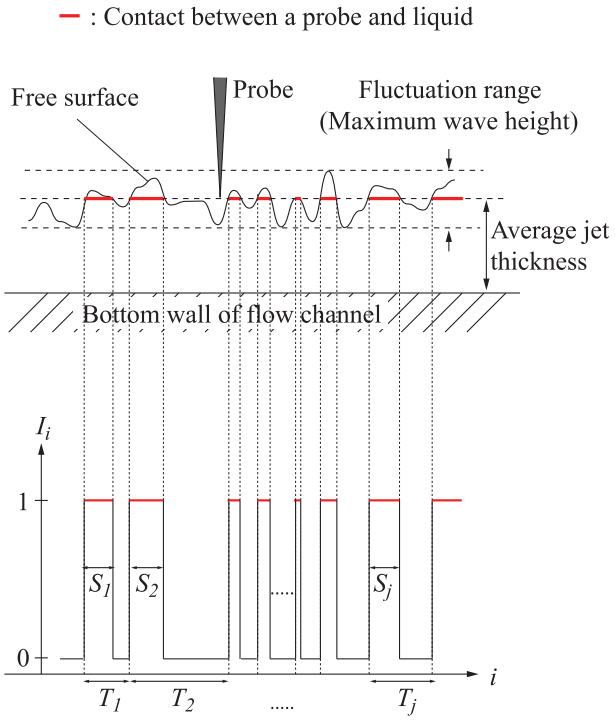

Fig. 10 Illustrative drawing of the contacts between the free surface and the probe tip and of their contact signals (T: contact period (wave period), S: contact duration). The height of the probe tip equals the average jet thickness. At this position, the contact period T can be defined as the wave period in the same manner as in the zero-up-crossing method [36].

recorded at each step. Therefore, this sensor provides information about surface fluctuations as ON–OFF signals at each probe position. The sensor is installed on a viewing port (in the figure, it is installed at port #2 located 175 mm downstream from the nozzle exit, and the spanwise position of the probe is set to the center of the flow channel).

Figure 10 illustrates the contacts between the free surface and the probe and their time-series contact signals I_i ($i = 1 - n$, where n denotes the number of signals) when the probe tip is located at the mean liquid level [12]. In the figure, the contact signals are digitized into 1 and 0 to indicate contact and no contact, respectively. In principle, as shown in Fig. 10, the time period between each contact at the mean liquid level is thought of in the same way as the wave period defined by the zero-up-crossing method that is used to define a "wave" in the random-phase/amplitude model [36] (this model is briefly explained later in this section). Therefore, the wave period T_j ($j = 1 - k$, where k denotes the number of contacts) can be obtained from the contact signals recorded at the mean liquid level. Then, histograms of the wave period and wave period distributions can be obtained.

Figure 11 presents the distribution of the non-dimensional wave period τ, which is defined as the wave period (T) divided by the mean wave period ($\overline{T}$), obtained

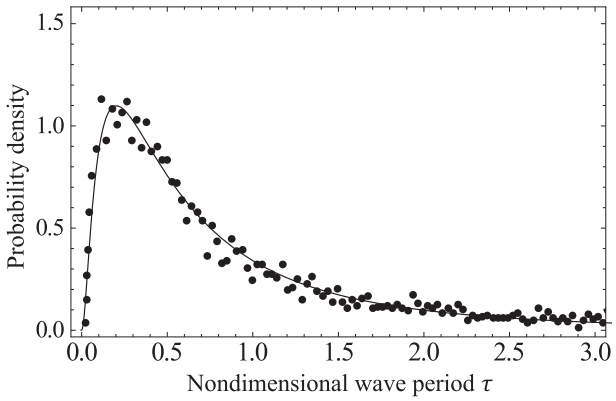

Fig. 11 Non-dimensional wave period distribution obtained 175 mm downstream from the nozzle exit in the Osaka University loop. The filled-in circles represent the experimental data. The solid line shows the log–normal distribution derived from the random-phase/amplitude model of ocean waves.

experimentally 175 mm downstream from the nozzle exit at a jet velocity of 15 m/s in the Osaka University loop [12]. The solid line was obtained from the following log–normal distribution:

$$p(\tau) = \frac{1}{\sqrt{2\pi}\delta\tau}\exp\left[-\frac{1}{2}\left(\frac{\log\tau - \mu}{\delta}\right)^2\right], \qquad (2)$$

where μ and δ denote the mean and standard deviation of $\log\tau$, respectively. As shown in the figure, the measured data agree well with the log-normal distribution. This distribution has its peak at $T < \overline{T}$. The measured results show that the surface waves are composed of waves with various wave periods but are dominated by high-frequency waves. Kitano *et al.* [37, 38] derived this distribution based on the random-phase/amplitude model.

Here, we outline the random-phase/amplitude model [36], which is a basic means of describing a random surface elevation. First, this model is based on the stochastic properties of the surface elevation rather than its hydrodynamic properties. The surface elevation at any one location and at any one moment in time is treated as a random variable (a variable whose exact value cannot be predicted). In other words, we do not attempt to determine an exact profile of the surface elevation by solving the deterministic Navier–Stokes equations. Second, in this model, the surface elevation is considered to be the sum of a large number of statistically independent, harmonic waves (a Fourier series), each with a constant amplitude and a phase randomly chosen for each realization of the time record. Third, this model is based on the assumption that the surface elevation is a stationary Gaussian process.

For such a process, Rice [39, 40] derived an analytical expression for the mean frequency of the level crossing in terms of the variance density spectrum, which shows how the variance of the sea-surface elevation is distributed over the frequencies of the wave components that create sur-

face fluctuations. With this expression, it can be shown that, for waves with a narrow spectrum, the wave height is Rayleigh-distributed with the zeroth-order moment of the wave spectrum as the only parameter. Observations at sea have shown that this is also the case for waves with a broader spectrum. Section 4.4 compares the experimentally obtained wave height distribution with the Rayleigh distribution.

For random ocean waves, the wave period distribution is as important as the wave height distribution because these distributions are representative of the wave properties as well as the frequency spectra [36]. In contrast to the wave height distribution, the wave period distribution is difficult to obtain theoretically. Ocean wave researchers have attempted to derive the wave period distribution theoretically [41–43]. However, as pointed out by Kitano, their theories have unrealistic features; in particular, the variances of the derived wave period distributions do not converge. With this lack of convergence in mind, Kitano [37, 38] derived the log–normal distribution empirically rather than deductively (based on the random-phase/amplitude model). The log–normal distribution is the best approximation of the experimentally obtained wave period distributions, as shown in Refs. [37,38]. We expect that a sound theory for deriving the log–normal distribution will be established in the near future. Log–normality itself is observed widely in turbulent flows (e.g., turbulent intermittency [44, 45] or low-speed streaks in the near-wall region of a turbulent boundary layer [46]). A log–normal process is the statistical realization of the multiplicative product of many independent random variables, each of which is positive. Therefore, the log–normality of the wave period distribution may arise from the interactions of many independent vortices underneath the free surface.

4.4 Wave height (amplitude)

In the development of the IFMIF Li target, the wave height (amplitude) is the most important wave parameter to be measured because a highly stable high-speed jet is required for IFMIF.

Wave heights can be measured using the contact probe and the LP method. In the following sections, methods of measuring wave height using both methods are described along with new interesting experimental results obtained in ELTL.

As illustrated in Fig. 9, the contact probe is scanned vertically step by step to obtain the contact signals at each step. From the obtained contact signals, a contact frequency, defined as the number of contacts per second, is calculated at each step. Then, a contact frequency profile, or the relationship between the contact frequency and the vertical probe position, is plotted. Finally, the differentiated contact frequency profile expresses the wave height distribution. Our previous studies contain detailed information concerning the method [9, 10].

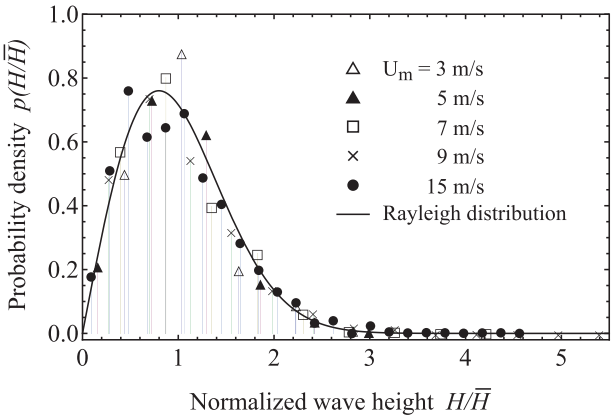

Fig. 12 Wave height distribution obtained 175 mm downstream from the nozzle exit in the Osaka University loop. The symbols indicate the experimental data at various jet speeds. The solid line represents the Rayleigh distribution, which was theoretically derived from the random-phase/amplitude model of ocean waves.

Figure 12 shows the non-dimensional wave height distribution obtained 175 mm downstream from the nozzle exit in the Osaka University Li loop. The horizontal axis denotes the non-dimensional wave height defined as the wave height (H) divided by the mean wave height ($\overline{H}$). The solid line represents the following Rayleigh distribution:

$$\mathrm{p}\left(\frac{H}{\overline{H}}\right) = \frac{\pi}{2}\frac{H}{\overline{H}}\exp\left[-\frac{\pi}{4}\left(\frac{H}{\overline{H}}\right)^2\right]. \quad (3)$$

As shown in Fig. 12, the experimental data agree well with the Rayleigh distribution. As mentioned in the previous section, it is well known in the field of ocean waves that the Rayleigh distribution is an accurate model and can be applied to the distribution of ocean wave heights [36]. We demonstrated for the first time that the Rayleigh distribution can also be applied to the distribution of Li wave heights despite the large differences between the surface tensions of water and Li (the surface tension of Li (at 250 - 300 °C) is approximately 5 times larger than that of water (at 20 °C)).

As explained in Sec. 4.3, the random-phase/amplitude model is based on the stochastic properties of the surface elevation. Furthermore, because the model was originally applied to the prediction of electrical noise [39, 40], it does not (explicitly) depend on the physical properties of the liquid (e.g., the parameter of the Rayleigh distribution is the zeroth-order moment of the wave energy spectrum). Based on these discussions and because the wave height and period distributions of Li are the Rayleigh and log–normal distributions, respectively, it is reasonable to believe that the Li surface elevation is also a stationary Gaussian process and that the random-phase/amplitude model applicable to ocean waves is also applicable to Li waves, irrespective of differences in the material properties

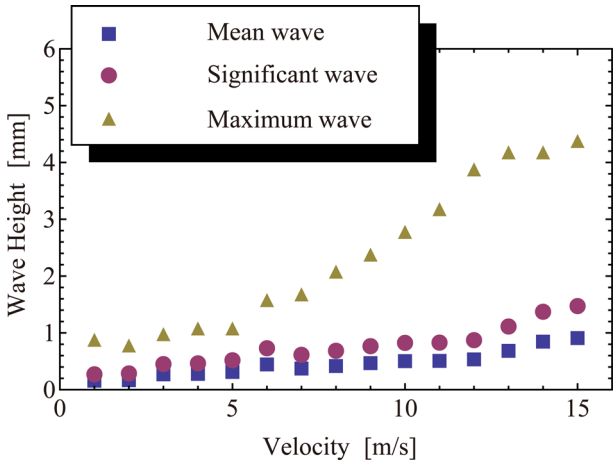

Fig. 13 Statistical wave height as a function of the mean jet velocity obtained at the Osaka University loop. All of the wave heights (the mean, significant, and maximum wave heights) monotonically increase with the mean jet speed.

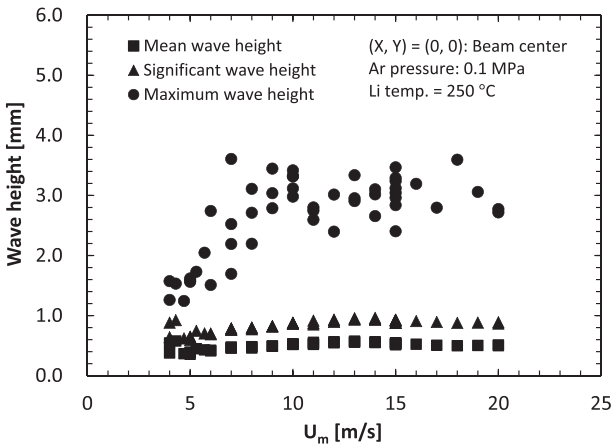

Fig. 14 Statistical wave height as a function of the mean jet speed obtained at ELTL. In contrast to the experimental results obtained at the Osaka University Li loop, at higher jet speeds, more than approximately 8 m/s, each statistical wave height reaches a plateau. This is advantageous for an IFMIF target because this result shows that the jet stability is unchanged within the IFMIF operating range (10 - 20 m/s).

of Li and water.

The random variables of the probability density functions (the log-normal and Rayleigh distributions), derived based on the random-phase/amplitude model, are non-dimensionalized using the mean values of the variables (see Eqs. (2) and (3)). Therefore, these functions yield the "relative" characteristics of the variables. In contrast, we expect that the "absolute values" of the statistical wave heights, such as the mean or maximum wave height, can be predicted using fluid mechanics because the surface elevation is generated according to fluid mechanics, not stochastic theory.

From the experimental data, we can obtain the mean, significant, and maximum wave heights [10]. Here, the mean wave height ($\overline{H}$) is the arithmetic mean of all of the wave heights, the maximum wave height is the full range of contact, and the significant wave height (H_s), which is said to be close to the average wave height estimated by the human eye, can be calculated to be $H_s \cong 1.6\overline{H}$.

Figure 13 illustrates the statistical wave heights obtained at the Osaka University loop [10]. The three wave heights increase monotonically with increasing mean nozzle-exit jet velocity. Thus, the flow stability decreases with increasing jet velocity. This behavior can easily be understood from the Fr and We numbers listed in Table 3. These numbers increase with the increasing characteristic velocity of the horizontal straight jet.

Figure 14 presents the statistical wave heights obtained at the IFMIF beam center under an Ar pressure of 0.1 MPa at a Li temperature of 250 °C at ELTL. This figure shows an interesting result. In contrast to the results obtained at the Osaka loop, the wave height reaches a plateau near 10 m/s as the mean jet speed increases. In addition, each statistical wave height obtained at ELTL is smaller than the corresponding statistical wave height obtained at the Osaka University Li loop. This difference is attributable to the effect of the centrifugal force. The centrifugal force is proportional to the square of the flow velocity; therefore, it is weak at low velocities. At the same time, the destabilizing effect of the inertia force is also proportional to the square of the velocity (see the definitions of the We and Fr numbers). At higher velocities, the magnitudes of the centrifugal and inertia forces become comparable, and the flow-stabilizing and -destabilizing effects are balanced. Therefore, flow stability becomes constant at higher velocities. This characteristic appears in the form of a constant Fr number, as in Table 4.

4.5 Average thickness

The average thickness uniformity of the Li target is crucial for IFMIF because it directly affects the spatial uniformity of the neutron flux distribution. Therefore, the average thickness, as well as the wave amplitude, is a key parameter to measure to validate the Li target. The average thickness can be measured using a contact probe and the LP method.

In measurements using a contact probe, the average thickness is defined as the peak position of the contact frequency profile [9]. By scanning the probe in the spanwise direction, a spanwise average thickness profile can be obtained, which enables the characteristics of stationary surface wake profiles to be examined. In a previous study, we showed that the inevitable surface wakes originating at the nozzle corners have negligible effects on the average thickness profile inside the IFMIF beam footprint [33]. Figure 15 shows the jet thickness distribution in

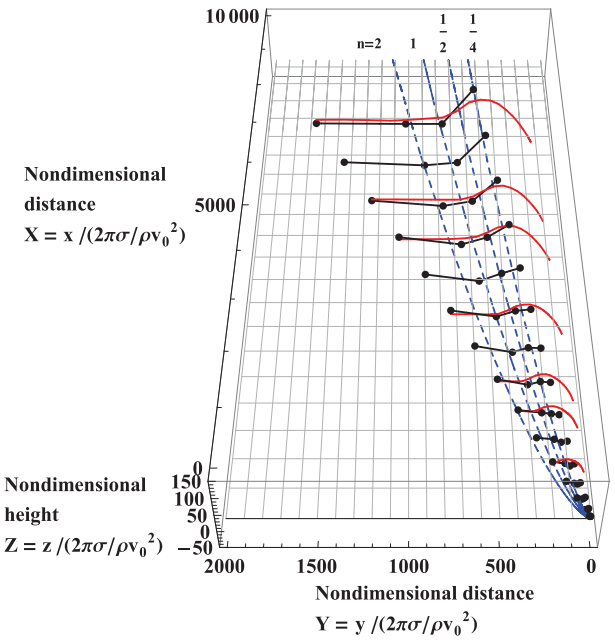

Fig. 15 Thickness distribution in non-dimensional space. Black dots indicate the experimental results obtained 175 mm downstream from the nozzle exit at four spanwise locations at various jet speeds; the dashed blue line represents the theoretical isophase lines of the free-surface wake for capillary waves, where $\boldsymbol{n}$ represents the phase difference (e.g., $\boldsymbol{n = 1}$ indicates a phase difference of $\boldsymbol{2\pi}$); and the bold red line shows the numerical calculation results (the contact angle between the wall and Li = 140°). The non-dimensionalization parameter $\boldsymbol{2\pi\sigma/\rho v_0^2}$ appears explicitly in the mathematical form of the theoretical isophase lines of the free-surface wake when only the capillarity is taken into account.

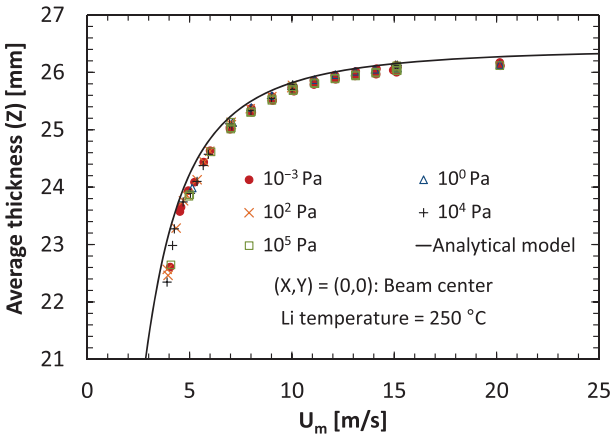

Fig. 16 Average thickness of the Li jet at the beam center at ELTL. The symbols correspond to the measurement results at various Ar gas pressures using the LP method, and the solid line shows the theoretically predicted jet thickness based on Bernoulli's theorem and the law of mass conservation. At a lower jet speeds, Li accelerates due to gravity. In contrast, at higher jet speeds, the gravitational acceleration becomes negligible, and the Li near the back wall decelerates due to a negative pressure gradient. Finally, the jet thickness approaches a plateau when the jet speed goes to infinity.

the non-dimensional space [33]. The x-, y-, and z-axes denote the streamwise, spanwise, and depth-wise directions, respectively. The position $(x, y) = (0, 0)$ corresponds to the corner between the nozzle edge and the side wall, and $z = 0$ corresponds to the bottom of the flow channel (the back wall). The three axes are non-dimensionalized using $2\pi\sigma/\rho v_0^2$ (v_0 is the mean jet speed). The experimental, numerical, and analytical results are shown in Fig. 15. The experimental results were measured using the contact probe in the Osaka University Li loop. The numerical results were obtained from a computational fluid dynamics calculation modeling the horizontal Li jet produced at the Osaka loop. The analytical results were taken from Ref. [47], in which the profile of a surface wake taking into account capillarity alone is formulated (known as the fish-line problem). The three results agree well, and the surface wake profile is predictable using analytical and numerical methods. Moreover, the wakes originating at the nozzle corners have negligible effects on the average thickness profile inside the beam footprint.

In measurements using the LP method, the average thickness is defined as the arithmetic mean of the time-series jet thickness data. The LP method is based on a laser distance meter, and measurement of the distance to the back wall is necessary to obtain the thickness information; the jet thickness can be calculated by subtracting the distance to the Li surface from the distance to the back wall. Figure 16 shows the average thickness measured at the beam center at ELTL [14]. The solid line represents the results of an analytical prediction of the average thickness characteristics. In the analysis, we assumed that the velocity and pressure profiles of the Li jet in the streamwise and depth-wise directions were linearly distributed under gravity, and we used Bernoulli's theorem and the law of conservation of mass to derive the formula for the average jet thickness. The experimental and analytical results agree closely. Similar to the wave height, the average thickness plateaus as the mean jet speed increases, because, as the mean jet speed increases, the flow acceleration due to gravity becomes negligible compared to the flow deceleration due to the static pressure increasing along the concave back wall, and the velocity profile becomes similar to those in high-velocity conditions (see Eq. (8) in [14]).

The LP method is a non-contact-type measurement method, and the distance can be measured from afar via a laser. From the viewpoint of application in IFMIF as a thickness monitoring device, this is very beneficial because the components around the target assembly will be heavily activated and available materials that can withstand such an environment are limited.

5. Summary

We began studies on a high-speed liquid Li wall jet for IFMIF in 2002. At that time, there were no diagnostics available to measure the Li jet characteristics. Since then, we have developed various diagnostic tools reviewed in this study and have revealed surface wave and wake characteristics generated on the Li jet, as well as the average thickness characteristics of the jet. As presented here, we have obtained sufficient information concerning the Li jet characteristics under "beam-off" conditions. The information required in the next stage to refine the IFMIF Li target design includes the Li jet characteristics under "beam-on" conditions, simulating deuteron beam irradiation.

Our achievements have contributed significantly to the development of the IFMIF Li target. Both the wave characteristics and the diagnostic tools can be applied not only to the IFMIF Li target but also to innovative liquid metal diverters or first walls in the field of fusion engineering as well as to liquid metal targets for high-power beams. We hope that our findings will also contribute to these applications.

Acknowledgments

This study contains the research results obtained during the KEP of IFMIF, the cooperative research with the National Institute for Fusion Science (NIFS05KOBF009), and the IFMIF/EVEDA project being pursued by Japan and Europe under the Broader Approach (BA) agreement. The authors express their gratitude to everyone involved in the development of the IFMIF Li target.

[1] T. Norimatsu *et al*., Fusion Sci. Technol. **56**, 361 (2009).
[2] Z. Kawara *et al*., Fusion Eng. Des. **85**, 2181 (2010).
[3] M.A. Abdou *et al*., Fusion Eng. Des. **54**, 181 (2001).
[4] R.E. Nygren *et al*., Fusion Eng. Des. **72**, 181 (2004).
[5] S.V. Mirnov *et al*., Plasma Phys. Control. Fusion **48**, 821 (2006).
[6] S. Smolentsev *et al*., Fusion Eng. Des. **85**, 1196 (2010).
[7] J. Knaster *et al*., Nucl. Fusion **53**, 116001 (2013).
[8] J. Knaster*et al.*, Nucl. Fusion **55**, 086003 (2015).
[9] T. Kanemura *et al*., Fusion Eng. Des. **82**, 2550 (2007).
[10] H. Kondo *et al.*, Fusion Eng. Des. **85**, 1102 (2010).
[11] T. Kanemura *et al*., J. Nucl. Mater. **417**, 1303 (2011).
[12] T. Kanemura *et al*., Fusion Eng. Des. **86**, 2462 (2011).
[13] T. Kanemura *et al*., Fusion Eng. Des. **89**, 1642 (2014).
[14] T. Kanemura *et al*., Fusion Eng. Des. **98–99**, 1991 (2015).
[15] H. Kondo *et al*., Fusion Eng. Des. **82**, 2483 (2007).
[16] H. Sugiura *et al.*, Fusion Eng. Des. **84**, 1803 (2009).
[17] H. Sugiura *et al*., J. Nucl. Sci. Technol. **48**, 1230 (2011).
[18] T. Kanemura *et al*., Fusion Eng. Des. (2016), doi:10.1016/j.fusengdes.2015.10.030
[19] N. Uda *et al*., J. Nucl. Sci. Technol. **38**, 936 (2001).
[20] H. Horiike *et al.*, Fusion Eng. Des. **66–68**, 199 (2003).
[21] H. Nakamura *et al*., in: Proceedings of Eighth International Topical Meeting of Nuclear Reactor Thermal Hydraulics (NURETH-8), Volume 3, pp.1268–1275, Kyoto, Japan, September 30–October 4, 1997.
[22] M. Ida *et al*., Fusion Eng. Des. **70**, 95 (2004)
[23] H. Kondo *et al*., Nucl. Fusion **51**, 123008 (2011).
[24] H. Kondo *et al*., Fusion Eng. Des. **86**, 2437 (2011).
[25] H. Kondo *et al*., in: Proceedings of 19th International Conference on Nuclear Engineering, ICONE19-43111, Chiba, Japan, May 16–19, 2011.
[26] T. Furukawa *et al*., Fusion Eng. Des. **86**, 2433 (2011).
[27] T. Furukawa *et al*., Fusion Eng. Des. **89**, 2902 (2014).
[28] H. Kondo *et al.*, Fusion Eng. Des. **75–79**, 865 (2005).
[29] K. Itoh *et al*., Fusion Technol. **36**, 69 (1999).
[30] J.A. Hassberger, in: Proceedings of 10th Symposium on Fusion Engineering, Volume 2, pp.1849–1853, Philadelphia, Pennsylvania, December 5–9, 1983.
[31] K. Itoh *et al*., Fusion Technol. **37**, 74 (2000).
[32] S. Yoshihashi-Suzuki *et al*., Fusion Eng. Des. **86**, 2577 (2011).
[33] H. Kondo *et al*., Fusion Eng. Des. **84**, 1086 (2009).
[34] H. Kondo *et al*., Fusion Eng. Des. **96–97**, 117 (2015).
[35] H. Kondo *et al*., Fusion Eng. Des. (2016), doi:10.1016/j.fusengdes.2015.09.016
[36] L.H. Holthuijsen, *Waves in Oceanic and Coastal Waters* (Cambridge University Press, New York, 2007).
[37] T. Kitano *et al*., Annu. J. Coast. Eng. **54**, 91 (2007) [in Japanese].
[38] T. Kitano *et al*., Annu. J. Coast. Eng. **55**, 121 (2008) [in Japanese].
[39] S.O. Rice, Bell. Syst. Tech. J. **23**, 282 (1944).
[40] S.O. Rice, Bell. Syst. Tech. J. **24**, 46 (1945).
[41] M.S. Longuet-Higgins, J. Geophys. Res. **80**, 2688 (1975).
[42] M.S. Longuet-Higgins, On the joint distribution of wave periods and amplitudes in a random wave field, Proc. Roy. Soc. Lond. A **389**, 241 (1983).
[43] P. Stansell *et al.*, J. Fluid Mech. **503**, 273 (2004).
[44] A.M. Obukhov, J. Fluid Mech. **13**, 77 (1962).
[45] A.N. Kolmogorov, J. Fluid Mech. **13**, 82 (1962).
[46] C.R. Smith and S.P. Metzler, J. Fluid Mech. **129**, 27 (1983).
[47] H. Lamb, *Hydrodynamics* (Cambridge University Press, Cambridge, Sixth edition, 1932) pp.468–471 (Art. 272).